

1 **Effects of bedrock lithology and subglacial till on the motion of Ruth Glacier, Alaska,**
2 **deduced from five pulses from 1973-2012**

3 **ABSTRACT**

4 A pulse is a type of unstable glacier flow intermediate between normal flow and surging. Using
5 Landsat MSS, TM, and ETM+ imagery and feature tracking software, a time-series of mostly
6 annual velocity maps from 1973 to 2012 was produced that reveals five pulses of Ruth Glacier,
7 Alaska. Peaks in ice velocity were found in 1981, 1989, 1997, 2003, and 2010; approximately
8 every 7 years. During these peak years the ice velocity increased 300%, from approximately 40
9 m/yr to 160 m/yr, and occurred in an area of the glacier underlain by sedimentary bedrock. Based
10 on the spatio-temporal behavior of Ruth Glacier during the pulse cycles, we suggest the pulses
11 are due to enhanced basal motion via deformation of a subglacial till. The cyclical nature of the
12 pulses is theorized to be due to a thin till, with low permeability, that causes incomplete drainage
13 of the till between the pulses, followed by eventual recharge and dilation of the till. These
14 findings suggest care is needed when attempting to correlate changes in regional climate with
15 decadal-scale changes in velocity, because in some instances basal conditions may have a greater
16 influence on ice dynamics than climate.

17

18

19 **INTRODUCTION**

20 **Ruth Glacier**

21 Ruth Glacier is a 58 km long alpine glacier in the Alaska Range of central Alaska, USA
22 (Figure 1), residing in a subarctic continental climate (Shulski and Mogil, 2009) with a
23 predominantly southern aspect. Ruth Glacier has a multi-lobed accumulation area consisting of a

24 West Fork, Northwest Fork, and North Fork. The headwall of the Northwest Fork reaches 4300
25 meters above sea level and is approximately 4 km from the summit of Mount McKinley, the
26 highest peak in North America. The separate lobes of the accumulation area converge at the head
27 of the Great Gorge, an approximately 12 km long, 1.5-2 km wide valley with 1500 m high steep-
28 sided walls that forms the upper ablation area between the 12 km and 26 km marks (Fig. 1). In
29 1983 the ice depth in the Great Gorge was measured using seismic methods and found to be up
30 to 1150 meters thick (unpublished data of K. Echelmeyer). The lower ablation area, below the
31 Great Gorge, is approximately 31 km long and 3-4 km wide and ends in a small piedmont lobe
32 roughly 8 km wide, which is partially covered by vegetation. The average ice surface slope
33 within the Great Gorge is 2.6° , and below the gorge the average ice surface slope is half as much,
34 1.3° , per the National Elevation Dataset (Gesch and others, 2009). At the base of the Great Gorge
35 there is some crevassing where the ice exits the gorge; the rest of the ablation area is free of
36 major crevassing (as seen in the 30-meter Landsat imagery used in this study), but the medial
37 moraines exhibit a slightly wavy pattern. The Great Gorge, and parts of the West Fork,
38 Northwest Fork, and lower ablation area are underlain by Tertiary (Paleocene) biotite-muscovite
39 granite and quartz monzonite of the McKinley Sequence (delineated by the red polygons and
40 denoted by the symbol Tpgr in Figure 1) (Reed and Nelson, 1980; Gamble and Reed, 1996). The
41 North Fork and the ablation area immediately below the Great Gorge are underlain by
42 sedimentary rocks from the Cretaceous and Jurassic periods (denoted as KJf in Figure 1). These
43 rocks are part of the Kahiltna Flysch Sequence and are comprised of argillite, fine to coarse
44 greywhacke, conglomerates, and thin layers of chert and limestone (Reed and Nelson, 1980;
45 Csejtey and others, 1992). Part of the piedmont lobe is underlain by Tertiary (Miocene)
46 sedimentary bedrock comprised of sandstone, siltstone, shale, and claystone of the Tyonek

47 Formation (delineated by the yellow dotted polygon and denoted as Tty in Figure 1), which is
48 part of the Kenai Group (Solie and others, 1991).

49 Little has been published concerning Ruth Glacier. Mayo (1978) notes Ruth Glacier is a
50 pulsing glacier and mentions the existence of small potholes in its surface that are the remnants
51 of large crevasses. Hall and Ormsby (1983) examined Ruth Glacier using Landsat Multispectral
52 Scanner and SEASAT synthetic aperture radar data from the summer of 1978 and noted the firn
53 zone was located within the Great Gorge. Heid and Kääb (2012a) produced velocity
54 measurements for nine glaciers in the Alaska Range using optical feature tracking methods and
55 noted only Ruth Glacier had accelerated during the period from 1986/87 to 2009/10; the zone of
56 acceleration was restricted to the ablation zone below the Great Gorge. Burgess and others
57 (2013) used synthetic aperture radar offset tracking to measure the wintertime speed of all
58 glaciers in the Alaska Range during the late 2000s; the exact year is not given for each glacier,
59 varying from 2007 to 2010. It was found that Ruth Glacier was moving at 0.6 to 1.0 m/day (219
60 to 365 m/yr) in the Great Gorge, with the ice gradually decelerating from approximately 0.5
61 m/day (182.5 m/yr) immediately below the Great Gorge to being stagnant at the terminus. Ward
62 and others (2012) note the igneous bedrock (Tpgr) of the Denali massif is significantly less
63 fractured than the surrounding tectonically deformed sedimentary bedrock (KJf and Tty).
64 Fracture spacing in the granitic bedrock is on the order of decimeters to hectometers, while
65 fracture spacing in the sedimentary bedrock is on the order of centimeters to decimeters. This
66 difference in fracture spacing causes a large difference in rates of glacier erosion (plucking)
67 between the two predominant bedrock types. The result is that the valley in which Ruth Glacier
68 resides tends to be narrow, with steep-sided walls (often 60° or greater in slope) in regions
69 underlain by the granitic bedrock (eg. The Great Gorge and between the 41 and 48 km marks),

70 and the valley tends to be wider with shallow-sloped walls (often 45° or less) when underlain by
71 sedimentary bedrock (Ward and others, 2012). Thus, the geometry of the glacier, and
72 consequently ice thickness and basal shear stress, are dictated partly by the underlying bedrock
73 type.

74 **Pulsing glaciers**

75 Mayo (1978) defines glacier pulses as periodic unstable flow that is lesser in magnitude
76 than surges, and therefore, pulsing glaciers are intermediate between normal and surging
77 glaciers. Pulsing glaciers may be identified by the existence of characteristic wavy medial
78 moraines, large-scale wavy foliation, or boudinage that may be present on only part of the
79 glacier, indicating only part of it pulses. If the characteristic pattern is continuous, it is suggested
80 the glacier experiences regular, periodic pulses. Mayo (1978) notes that potholes (remnants of
81 crevasses) probably form in the zone of ice loss on pulsing glaciers. Approximately 140 glaciers
82 in Alaska have been identified with these characteristics in aerial photography from the 1960s
83 and 1970s by Austin Post and L.R. Mayo. Most of these pulse-type glaciers occur in the same
84 regions as surge-type glaciers, in the Alaska Range, Chugach Mtns., St. Elias Mtns., and
85 Wrangell Mtns. Pulsing behavior may occur in conjunction with the drainage of large glacier-
86 dammed lakes, suggesting a link between basal hydrology and pulsing flow. Mayo (1978) lists
87 some pulsing glaciers and the dates of their observed pulses: West Gakona Glacier (1949),
88 Nizina Glacier (1961), Trident Glacier (1970, 1971), MacLaren Glacier (1971, 1972), and
89 Tokositna Glacier (1971, 1972). Additionally, undated pulses are listed for: Capps Glacier,
90 Eureka Glacier, Hayes Glacier, Kahiltna Glacier, Miles Glacier, Ruth Glacier, Sanford Glacier,
91 and the West Branch of Sheridan Glacier.

Sometime between 1974 and 1977 Trapridge Glacier, Yukon Territory, Canada, began a prolonged surge that lasted until 2005 (Frappé and Clarke, 2007). During the surge a string of five 4-year pulses were detected from 1981 to 2002, with amplitudes of roughly 10 m/yr, a 33% increase in velocity. Trapridge Glacier is a polythermal glacier with temperate upper ice and subzero basal ice, and it is underlain by a deformable, permeable till up to 10 m thick (Blake and others, 1992; Stone, 1993). Increased ice velocity during the surge, and by inference during the pulses, is attributed to sliding at the bed caused by failure of the basal till. Till failure reduces basal friction and transfers stress laterally to the glacier margins, thereby producing an area of plug-flow along the central portion of the glacier, allowing ice there to accelerate. During a similar time frame, from approximately 1980 to 2002, Black Rapids Glacier, a temperate glacier in the central Alaska Range (Harrison and others, 1975), experienced two consecutive 12-year pulses, with amplitudes of roughly 20-25 m/yr, representing velocity increases of 55-65% (Nolan, 2003). Black Rapids Glacier is underlain by a till 5-7 m thick (Nolan and Echelmeyer, 1999), and it has been shown via borehole tiltmeter measurements that up to 70% of the ice velocity during the pulses was due to deformation within the till at depths >2 m below the ice/till interface (Truffer and others, 2000). Again, it was theorized that till failure reduced stresses in the center of the glacier and transferred them towards the margins. This process promotes increased basal motion along the glacier centerline and increased ice deformation near the margins (Truffer and others, 2001; Nolan, 2003).

Ice dynamics influence the length, area, and volume of a glacier. Changes in ice dynamics, therefore, necessarily result in changes in the geometry of a glacier, which in turn affects its mass balance. For example, pulses and surges may rapidly transfer ice to lower altitudes where it is subject to increased air temperature and ablation, thereby promoting a

115 reduction in mass balance. Knowing that dynamic instabilities such as pulses and surges are
116 intimately tied to the basal conditions of a glacier, an improved understanding of the relationship
117 between basal conditions and ice dynamics will further our understanding of the influences on a
118 glacier's mass balance. In this study we will examine the cyclical dynamic behavior of Ruth
119 Glacier to determine the amplitude, frequency, and spatial extent of its pulses. Based on the
120 spatial and temporal structure of the velocity fields during multiple pulse cycles, we will infer the
121 basal conditions beneath Ruth Glacier and describe the influence of bedrock lithology on the
122 behavior of its pulses.

123

124 **METHODS**

125 **Optical feature tracking**

126 Optical feature tracking methods were used to produce a time-series of ice surface
127 velocity maps spanning 1973-2012 for Ruth Glacier in order to delineate its periodic dynamic
128 behavior. COSI-Corr feature tracking software (Leprince and others, 2007) was used in
129 conjunction with Landsat Multispectral Scanner System (MSS), Thematic Mapper (TM), and
130 Enhanced Thematic Mapper Plus (ETM+) imagery to produce the velocity maps (see Table 1 for
131 image dates). COSI-Corr was chosen due to its proven precision (Scherler and others, 2008; Heid
132 and Kääb, 2012b), its ability to produce accurate displacement measurements in areas of low
133 contrast or with light cloud cover (Heid and Kääb, 2012b), and its ease of use. COSI-Corr
134 produces an intitial estimate of the displacement of features between sequential images by use of
135 the Fourier Shift Theorem which states the displacement is found in the phase portion of the
136 normalized cross power spectrum computed from the Fourier transform of each image
137 (Shekarforoush and others, 1996). Equal-sized subsets from each image centered on the same

138 pixel, called reference and search windows, corresponding to the temporally first and second
139 images, respectively, are matched to one another and a displacement measurement produced with
140 1-pixel accuracy. A re-weighted least squares phase minimization algorithm is then applied to
141 determine the final displacement. This algorithm minimizes the phase difference between the
142 initial displacement estimate and an ideal theoretical one, thus producing subpixel accuracy. This
143 process is repeated in a grid-like pattern across the entire image, producing individual
144 displacement measurements at predefined intervals. The displacement measurements (vectors)
145 produced by COSI-Corr are post-processed using a neighborhood analysis routine to remove
146 erroneous vectors. Any vector that is more than ± 2 standard deviations away from the mean
147 magnitude or direction of its local neighborhood, consisting of at least nine adjacent vectors, is
148 deemed an anomaly and removed. Afterwards, the vector field is visually inspected and any
149 remaining anomalies are manually removed. The individual vectors are interpolated using a
150 linear inverse-distance weighting scheme to produce a velocity raster. In May, 2003, the scan-
151 line correction mirror of Landsat-7 ETM+ failed, resulting in data voids in images acquired
152 afterwards; these images are commonly called SLC-off images. Fortunately, the portion of Ruth
153 Glacier in which the pulses are tracked (the ablation zone below the Great Gorge) lies near the
154 center of the Landsat-7 images where the data voids do not exist. Therefore, more advanced
155 feature tracking techniques, such as Ahn and Howat's (2011) null exclusion method or
156 orientation correlation (Fitch and others, 2002; Haug and others, 2010) were not necessary when
157 using SLC-off images for Ruth Glacier.

158 **Accuracy**

159 The accuracy of the velocity fields produced from feature tracking algorithms depends
160 on the precision of the matching method and how well the two images being matched are aligned

161 to one another. Heid and Kääb (2012b) evaluated the precision of COSI-Corr using Landsat-7
162 ETM+ 15-meter panchromatic imagery and found the root mean square error (RMSE) of its
163 displacement measurements to be ± 0.9 meters in the x-direction and ± 0.8 meters in the y-
164 direction, for a total RMSE of ± 1.2 meters, or ± 0.08 pixels. If we apply this same error (± 0.08
165 pixels) to 30-meter imagery, the expected error is ± 2.4 meters, and for 60-meter imagery the
166 expected error is ± 4.8 meters. Storey and Choate (2004) have shown the RMSE of the geometric
167 accuracy of Landsat-5 TM data is ± 5.5 meters (± 0.2 pixels), and Lee and others (2004) showed
168 the average geometric error of Landsat-7 ETM+ imagery is less than ± 5 meters ($\pm 0.16\bar{6}$ pixels).
169 Table 2 (last column) shows the listed geometric accuracy for each Landsat image used in this
170 study, upon receipt from the U.S. Geological Survey; the mean of the 22 values for TM/ETM+
171 images is 0.16 ± 0.04 pixels (4.8 ± 1.2 meters) (mean ± 1 standard deviation), which compares
172 well with the values given by Storey and Choate (2004) and Lee and others (2004). For the 12
173 MSS images, the mean geometric error is 0.47 ± 0.12 pixels (28.2 ± 7.2 meters).

174 For each image pair vectors on dry, snow-free, cloud-free land were analyzed to
175 determine the mean georeferencing error between the two images (Table 2). The average of these
176 mean georeferencing errors is 0.22 ± 0.09 pixels (7.0 ± 3.0 meters) for 30-meter TM and ETM+
177 imagery and 0.45 ± 0.15 pixels (24.1 ± 6.7 meters) for MSS imagery. The mean georeferencing
178 error for each image pair was subtracted from the on-ice vectors to improve the accuracy of the
179 velocity fields. The mean georeferencing error was also subtracted from the off-ice vectors,
180 resulting in a residual error between images which represents their final misalignment (Table 2).
181 We note the average of the mean residual errors for the TM/ETM+ image pairs, 0.15 ± 0.07
182 pixels (4.9 ± 2.6 meters), compares well with values quoted above by Storey and Choate (2004),
183 Lee and others (2004), and with the mean geometric accuracy for an individual image. Thus,

184 after removal of the mean georeferencing error, the TM/ETM+ image pairs are aligned to one
185 another as precisely as each individual image is aligned to the ground control points used to
186 geolocate it. We also note the image-to-image misalignment for each TM/ETM+ image pair is
187 within one standard deviation of the precision of COSI-Corr (± 0.08 pixels), which suggests that
188 after removal of the mean georeferencing error the residual misalignment of the TM and ETM+
189 image pairs approaches the limits of detection by COSI-Corr. The mean georeferencing error for
190 MSS data, as measured by COSI-Corr (Table 2) is 0.45 ± 0.15 pixels (24.1 ± 6.7 meters), and
191 after removal of this error, the residual image-to-image misalignment is 0.25 ± 0.07 pixels (14.1
192 ± 4.2 meters). Thus, after removal of the georeferencing error, the MSS image pairs are aligned
193 more precisely to one another than each individual image was originally aligned to its ground
194 control points upon receipt from the U.S. Geological Survey (compare the average residual error
195 of 0.25 pixels to the average geolocation error of 0.47 pixels). Using the root sum of squares
196 method, we estimate the combined error in the velocity fields, resulting from the mean residual
197 error and COSI-Corr's precision, to be 5.1 meters (0.17 pixels) for the 30-meter Landsat
198 TM/ETM+ data, and 15.7 meters (0.26 pixels) for the 60-meter Landsat MSS data.

199

200

201

202 RESULTS

203 COSI-Corr was unsuccessful in producing reliable displacement measurements within the
204 Great Gorge and in the accumulation area due to snow cover and a lack of surface features to
205 track, but it was quite successful below the Great Gorge. A time-series of 29 velocity maps
206 (Figures 2 to 5) shows the evolution of the pulses of Ruth Glacier in time and space, below the

207 Great Gorge. From 1973-74 to 1976-77 (Fig. 2a-c) much of the ablation area below the Great
208 Gorge is moving at 75 m/yr or less. Then in 1977-78 (Fig. 2d) the ice down to the 30 km mark
209 accelerates to almost 200 m/yr. In 1978-80 (Fig. 2e) the ice between the 35 km and 40 km marks
210 has accelerated relative to previous years, and by 1980-81 (Fig. 2f) all the ice down to the 45 km
211 mark has accelerated, much of it moving 150 m/yr or more, indicating a doubling of ice velocity
212 compared to the period from 1973 to 1977. From 1981-1982 (Fig. 2g) to 1983-84 (Fig. 3a), the
213 glacier gradually decelerates and returns to its pre-pulse velocity. In Figure 3 there are two pulses
214 evident between 1984-85 and 1995-99 that show a similar pattern of gradual acceleration and
215 deceleration of the ice, with peak velocities in 1987-91 (Fig. 3e) and 1995-99 (Fig. 3h). Due to
216 lack of cloud-free imagery between 1987 and 1991, and lack of data acquisition during the late
217 1990s, these pulses are not well defined in time, but it is clear the two pulses did occur due to the
218 increased velocities during these four-year time spans. From 1999-00 to 2001-02 (Fig. 4) the
219 cyclical pattern has continued, with a gradual increase in velocity from roughly 50-75 m/yr in
220 1999-00 (Fig. 4a) to >100 m/yr in 2001-02 (Fig. 4c) between the 26 and 35 km marks. By 2002-
221 03 (Fig. 4d) velocity reached a peak, with characteristic values of 150-200 m/yr between the 26
222 and 42 km marks, indicating the ice has more than doubled its speed compared to three years
223 earlier. Afterwards, the ice decelerates to its pre-pulse velocity by 2005-06 (Fig. 4g). A fifth
224 pulse is evident in Figure 5, which shows an acceleration of the ice from 2006-07 (Fig. 5a) to
225 2009-10 (Fig. 5d), with the peak being in 2009-10, followed by deceleration in 2010-11 and
226 2011-12 (Fig. 5e,f). Characteristic peak ice velocities during this last pulse, between the 26 and
227 42 km marks, are 150-200 m/yr, indicating a three- to four-fold increase in velocity compared to
228 2006-07.

229 To help illustrate the evolution of the pulses through time, the velocity at two points
230 along the glacier, 36 km and 43 km, are plotted in Figure 6. This graph clearly illustrates the
231 periodic nature of the pulses and highlights the five individual peaks. It should be noted that for
232 plotting purposes, velocity was assigned to the 2nd year of each image pair used to produce a
233 velocity field, or in the case of the 1987-91 and 1995-99 velocity fields, velocity was assigned to
234 a middle year, 1989 and 1997, respectively. Inspection of this graph yields characteristic pulse
235 amplitudes (peak value minus trough value) in excess of 120 m/yr (a 300% increase in velocity)
236 at the 36 km mark, and 60-70 m/yr (a 50-75% increase in velocity) at the 43 km mark for the
237 1981, 2003, and 2010 peaks. The amplitudes of the 1989 and 1997 pulses are not as great
238 because their respective velocity fields were produced using image pairs spanning four years,
239 thus the peak velocity values are averaged with surrounding years resulting in lower amplitudes.
240 Based on the occurrence of the peaks as described here, the pulses of Ruth Glacier have a
241 characteristic period of approximately 7 years.

242 To further aid in analyzing the pulses, longitudinal profiles of velocity, acceleration, and
243 strain rate were produced for each velocity field (Figures 7-10). The longitudinal velocity and
244 acceleration profiles in Figures 7a and 7b clearly show the extent of the pulse from 2009 to 2011.
245 All the ice below the Great Gorge down to roughly the 52 km mark noticeably accelerated during
246 this time. It is worthwhile to note that in the area of the 27 km mark, the 40-42 km marks, and
247 the 49 km mark, there are inflections in velocity and acceleration, and prominent peaks (or
248 troughs) in strain rate in 2009-10, 2010-11, and 2011-12. The location of these inflections, peaks,
249 and troughs approximately coincide with the transition from granitic to sedimentary bedrock at
250 the 28 km mark, a change from sedimentary to granitic bedrock at the 41 km mark, and a change
251 back to sedimentary bedrock at the 48 km mark, as seen in Fig 1. Examination of the

acceleration profiles (Fig. 7b) reveals the ice from the 26 km mark to roughly the 50 km mark accelerates (in varying amounts) simultaneously; there is no evidence of a wave front propagating downglacier. The strain rate between the 37 and 43 km marks changes from predominantly compressive before the pulse, to tensile during the pulse, and back to compressive afterwards; again, indicating the ice in this area is responding simultaneously to applied stresses.

The longitudinal profiles in Figure 8 span the years 1999 to 2006 and highlight the behavior of Ruth Glacier immediately before, during, and after the 2002-2003 pulse. As with the 2009-2010 pulse, there are noticeable inflections in velocity and acceleration, and noticeable peaks or troughs in strain rate, near the transitions between granitic and sedimentary bedrock at 28 km, 41 km, and 48 km. Again, it is evident that the entire stretch of ice between 26 and 50 km has accelerated simultaneously, and the same pattern of changing strain rate, from compressive to tensile, and back to compressive, is evident before, during, and after the pulse, respectively. The 2003-04 acceleration profile (Fig. 8b) shows a well-defined area of acceleration between the 42 and 50 km marks, atop granitic bedrock; this same area also increased in acceleration in 2010-11 (Fig. 7b) while the rest of the ice upglacier decelerated. Both of these acceleration events occurred one year after, and downglacier, of the peak pulse events in 2003 and 2010, which occurred atop sedimentary bedrock. Figure 9 shows the longitudinal profiles for the years surrounding, and including, the 1987-91 and 1995-99 pulses. Although these two pulses are not as well defined as the 2002-03 and 2009-10 pulses, the same patterns are still evident. There are inflections in the velocity and acceleration profiles (Fig. 9a,b), and peaks or troughs in the strain rate (Fig. 9c), near the same locations as the later pulses, at 26 km, 40-42 km, and 50 km. Again, large portions of the ice between the 26 and 50 km marks accelerate and decelerate in unison. During the 1987-91 and 1995-99 pulses, there is no obvious acceleration of the ice between the

275 42 and 50 km marks (Fig. 9b) (as seen in the later pulses (Fig. 7b, 8b)), probably due to the poor
276 temporal resolution of these two pulses. Lastly, Figure 10 shows the longitudinal profiles for the
277 years surrounding, and including, the 1980-81 pulse. Again, inflection points in the velocity and
278 acceleration profiles are seen at, or near, the 26 km, 40-42 km, and 50 km marks (Fig. 10 a,b),
279 but the pattern of peaks and troughs in strain rate seen in the other pulses is not clear.

280

281 **DISCUSSION**

282 To place our results in context with other surging and pulsing glaciers, we briefly discuss
283 till deformation and flow instabilities with regards to glacier dynamics. In turn, these discussions
284 help identify the likely basal conditions of Ruth Glacier during its pulses.

285 **Glacier motion by till deformation**

286 The location of surging glaciers in Svalbard is positively correlated with areas of fine-
287 grained sedimentary bedrock, which are easily eroded (Jiskoot and others, 2000), while in NW
288 North America surging glaciers are often found in fault-shattered valleys (Post, 1969). Glaciers
289 atop these areas are more likely to develop a soft bed than when atop intact crystalline
290 metamorphic or igneous bedrock. Sedimentary bedrock will produce a fine-grained till that will
291 have a low permeability which may be more prone to instabilities (Murray and Porter, 2001).
292 Instability within a till may develop due to decreased effective pressure, via increased basal
293 water input. As long as the discharge of water at the glacier bed is small, steady-state water
294 pressure will approximate ice overburden pressure and the water will flow by Darcian transport
295 through the till, or by a uniform water film at the base of the ice, and the till will remain
296 consolidated. When pore-water pressure in the till equals or exceeds ice overburden pressure the
297 till weakens and may dilate (Willis, 1995). Dilation of the till causes porosity and permeability to

298 increase, thus decreasing water pressure and shear strength (Murray, 1997). When a till dilates it
299 can no longer support shear stress and it deforms, allowing the glacier to accelerate. The
300 increased ice motion may occur as slip at the ice/till interface in which shear strain in the till
301 occurs in the uppermost layer of sediment. Shear strain may also occur within the till along a
302 plane of weakness, or it may be distributed throughout the till by the process of dilatant
303 hardening. When a till dilates, pore volume increases, allowing water to flow towards the
304 opening pores in the dilating sediment. If the rate of dilation is greater than the rate of pore-water
305 flow then water pressure will decrease in the dilated sediment and it will harden (Reynolds,
306 1885). When the shear band hardens, the strain is focused elsewhere within the till; thus, the
307 strain is distributed from one plane of weakness to the next.

308 Truffer and others (2000) suggest surges could be triggered by widespread dilation of
309 basal till as shear stresses exceed a critical value, along with attainment of a glacier geometry
310 that produces large basal shear stresses. Failed tills are concentrated under thicker ice, such as
311 along the glacier centerline, where driving stress is greatest and may exceed till yield strength.
312 Nolan (2003), when investigating the behavior of Black Rapid Glacier, proposed the idea of
313 waves of till failure (activation waves) that propagate underneath a glacier as follows: 1) Failed
314 till along a section of glacier centerline causes increased stress laterally and longitudinally
315 because the driving stress is redistributed elsewhere; 2) The glacier speed increases locally due to
316 failed till; 3) When the driving stress is distributed elsewhere, any till that was at, or near, a point
317 of failure will fail, thus increasing the area of the glacier with increased speed; 4) This process
318 creates a wave of till failure and subsequent ice motion that propagates downglacier via a
319 positive feedback loop by continuously placing increased stress on the downglacier till; 5) As the
320 area of failed till increases longitudinally, the glacier moves faster everywhere because of

321 reduced bed friction and greater basal motion. A similar mechanism was discussed by Frappé
322 and Clarke (2007) to explain the surge of Trapridge Glacier. The till deformation paradigm
323 allows glacier velocity to increase greatly without requiring large changes in glacier geometry or
324 the subglacial hydraulic system, assuming the till is near its failure threshold (Truffer and others,
325 2001).

326 Fowler and others (2001) noted that if the till layer has a low transmissivity (i.e. the till is
327 thin) and low permeability then oscillations in effective pressure, ice thickness, and ice flux can
328 occur. Ice speed during a pulse depends primarily on basal roughness. If the basal roughness is
329 large, then ice flow is sufficiently restricted to allow oscillatory behavior to occur; otherwise, a
330 major surge can occur if the basal roughness is small, because there is little restriction to ice
331 flow. Fowler and others (2001) also suggest that if a glacier is temperate and resides atop a thin
332 till, the ice may activate (i.e. the till fails beneath it) before any significant ice motion because
333 the activation waves are faster than the ice motion; so, the ice slumps forward rapidly moving as
334 a block, or plug. Therefore, there is no surge front that would otherwise separate fast-moving
335 surging ice and slow-moving quiescent ice. Plug flow has been observed on Black Rapids
336 Glacier (Harrison and Post, 2003) and Trapridge Glacier (Frappé and Clarke, 2007), both of
337 which have surged atop a till. Once a surge has been initiated by till failure, less stress is required
338 to keep the till in a failed state, allowing the surge to continue. This occurs because drag at the
339 glacier base increases longitudinal shear stress that might cause a till to fail even when water
340 pressures are less than the critical Coulomb threshold (Boulton and others, 2001). The
341 accelerated ice motion will cease when the ice can no longer be shoved forward by driving
342 stresses, either by obstacles restricting down glacier movement or by decreased upglacier
343 stresses, then the basal shear stress decreases below the till failure point and the till heals. Or, the

344 accelerated ice motion will cease if drainage of water from the till occurs, reducing water
345 pressure and allowing the till to heal. However, a till with low permeability may not drain
346 completely; thus, the till may not fully heal and it is left primed for another pulse episode when
347 enough water is introduced again (Nolan, 2003). A thin till, which has lesser water storage
348 capacity than a thick till, will refill quickly and surpass its Coulomb failure threshold sooner than
349 a thick till would, resulting in more frequent pulses.

350 **Basal conditions beneath Ruth Glacier**

351 Knowing that the sedimentary bedrock beneath Ruth Glacier is highly fractured and
352 easily eroded, and the fact that Ruth Glacier exhibits a dynamic behavior similar to other glaciers
353 known to reside atop deformable tills by accelerating and decelerating in a cyclical, plug-like
354 fashion, it seems likely a deformable till exists beneath Ruth Glacier between the 28 km and 41
355 km marks. The area from the 41 km mark to the 48 km mark is underlain by granitic bedrock that
356 will not as readily erode to produce a till, but there is likely some sediment beneath the glacier in
357 this area that was transported from above, but which is spatially sparse and does not promote
358 widespread increased ice motion via till dilation and deformation. The fact that the ice in this
359 area (lying atop the granitic bedrock) has accelerated during the pulses, although to a lesser
360 degree than ice atop sedimentary bedrock, is likely due to stress transfer and longitudinal
361 coupling with the ice upglacier (note the lesser velocity at the 43 km mark in Fig. 6 compared to
362 the 36 km mark). The inferred existence of a deformable till requires the basal ice and the till to
363 be at the pressure-melting point; therefore, we conclude Ruth Glacier is warm-based below the
364 Great Gorge. The simultaneous acceleration of the ice from the 26 km mark, immediately below
365 the Great Gorge, to roughly the 50 km mark, and the lack of a wave front, provide further
366 evidence that Ruth Glacier is warm-based in this area, because Fowler and others (2001) theorize

367 temperate glaciers atop deforming tills will slump forward, thus no wave front forms. The lack of
368 a wave front is in contrast to observations of typical Alaska-style surging glaciers wherein a
369 surge front separates quiescent ice from surging ice, as noted on Variegated Glacier (Kamb and
370 others, 1985) and Bering Glacier (Roush and others, 2003; Turrin and others, 2013). The
371 dynamic oscillating (pulsing) behavior of Ruth Glacier suggests the till is thin with a low
372 permeability (Fowler and others, 2001).

373 **Distinguishing pulses from surges**

374 Alaska-style surges are controlled by the morphological evolution of the basal drainage
375 system beneath temperate ice from a channelized system to a distributed cavity system (Kamb
376 and others, 1985) and are traditionally assumed to occur atop a hard bed. Svalbard-style surges
377 are controlled by the thermal evolution of the basal ice from sub-freezing to temperate (Fowler
378 and others, 2001; Murray and others, 2003) and occur atop a soft bed (a basal till). Both Alaska-
379 style and Svalbard-style surges can result in a surge front (kinematic wave) moving downglacier
380 that separates quiescent ice, moving primarily by internal deformation of the ice column, from
381 surging ice that moves primarily by slip at the ice/bed interface, or by deformation within a basal
382 till (in the case of a Svalbard-style surge). Pulses are controlled by the evolution of the basal till
383 from a healed state to a dilated state, and occur where the base is at the pressure-melting point. If
384 the till beneath Ruth Glacier froze between pulses, then a surge front would form in the manner
385 of a typical Svalbard-style surge during each pulse, but the lack of any wave front suggests the
386 base is perennially warm. As noted above, Trapridge Glacier experienced five low-amplitude
387 pulses during a prolonged surge (Frappé and Clarke, 2007), and Black Rapids Glacier, also a
388 surge-type glacier, experienced two low-amplitude pulses during quiescence (Nolan, 2003).
389 These studies suggest pulsing is a dynamic behavior apart from typical surging that may occur

390 either during an active, low-amplitude surge or during quiescence. Ruth Glacier is not known to
391 surge in the traditional sense, so pulsing may also occur on glaciers other than surge-type that
392 have the requisite warm base and till, and adequate shear stress and basal water pressure to dilate
393 the till.

394 **Implications for decadal-scale velocity measurements**

395 As mentioned above, Heid and Kääb (2012a) noted Ruth Glacier accelerated between
396 1986/87 and 2009/10. This perceived acceleration is a result of the years chosen for use in their
397 velocity determinations. The 1986/87 period falls between pulses, while the 2009/10 period is at
398 the peak of a pulse (Fig. 3), thus there is a perceived acceleration of >120 m/yr during this
399 period. If one had instead chosen images acquired in 1980/81 and 2007/2008 and performed the
400 same analysis, the result would be a deceleration of >-120 m/yr, the opposite of what Heid and
401 Kääb (2012a) reported. In either case, the pulses which occurred during the interval between
402 velocity measurements are missed. Optical feature tracking methods have now matured to the
403 point where decadal-scale regional, and perhaps global, studies of ice dynamics are possible, as
404 exemplified by Heid and Kääb (2012a). When performing such work, it is important to be aware
405 of any surging or pulsing glaciers in the chosen study area and how their periodic behavior might
406 affect results. In some instances, such as on Ruth Glacier, basal conditions may exert a greater
407 influence on ice dynamics than regional changes in climate on annual and decadal time frames.

408

409 **CONCLUSIONS**

410 From 1973 to 2012, a span of 39 years, Ruth Glacier experienced five pulses that have
411 gone unnoticed until now. These pulses are of low amplitude compared to typical surges of
412 glaciers in Alaska, and they occur without causing an advance of the terminus and without

413 widespread crevassing, perhaps helping to explain their oversight. The pulses have occurred on a
414 regular basis, approximately every seven years, with peaks in 1981, 1989, 1997, 2003, and 2010,
415 and with increases in ice velocity of >120 m/yr during the peaks in 1981, 2003, and 2010. The
416 pulses occur in an area of the glacier underlain by sedimentary bedrock, and we suggest that the
417 pulses are a result of enhanced basal motion due to deformation of a subglacial till. Therefore,
418 we infer that the base of Ruth Glacier, in the area in which the pulses occur, must be temperate.
419 Additionally, theory predicts that the manner in which the glacier moved during the pulses, with
420 a 20 km section of ice accelerating and decelerating in unison, and the lack of a wave front, is
421 suggestive of a perennial temperate base (Fowler and others, 2001). The oscillating dynamic
422 behavior is theorized to be due to a thin till with low permeability that is just above a critical
423 value (Fowler and others, 2001). The basal roughness is theorized to be great enough to restrict
424 ice flow and prevent the occurrence of major surges. These findings illustrate the influence of
425 bedrock lithology and a glacier's basal thermal regime on its dynamics, the combination of
426 which will ultimately affect its mass balance.

427

428 **ACKNOWLEDGEMENTS**

429 This project was funded by NASA grants NNX08APZ76 and NNX08AX88G. We thank Peter
430 Haeussler of the U.S. Geological Survey for providing information on the geology of the Mount
431 McKinley area.

432

433 **REFERENCES**

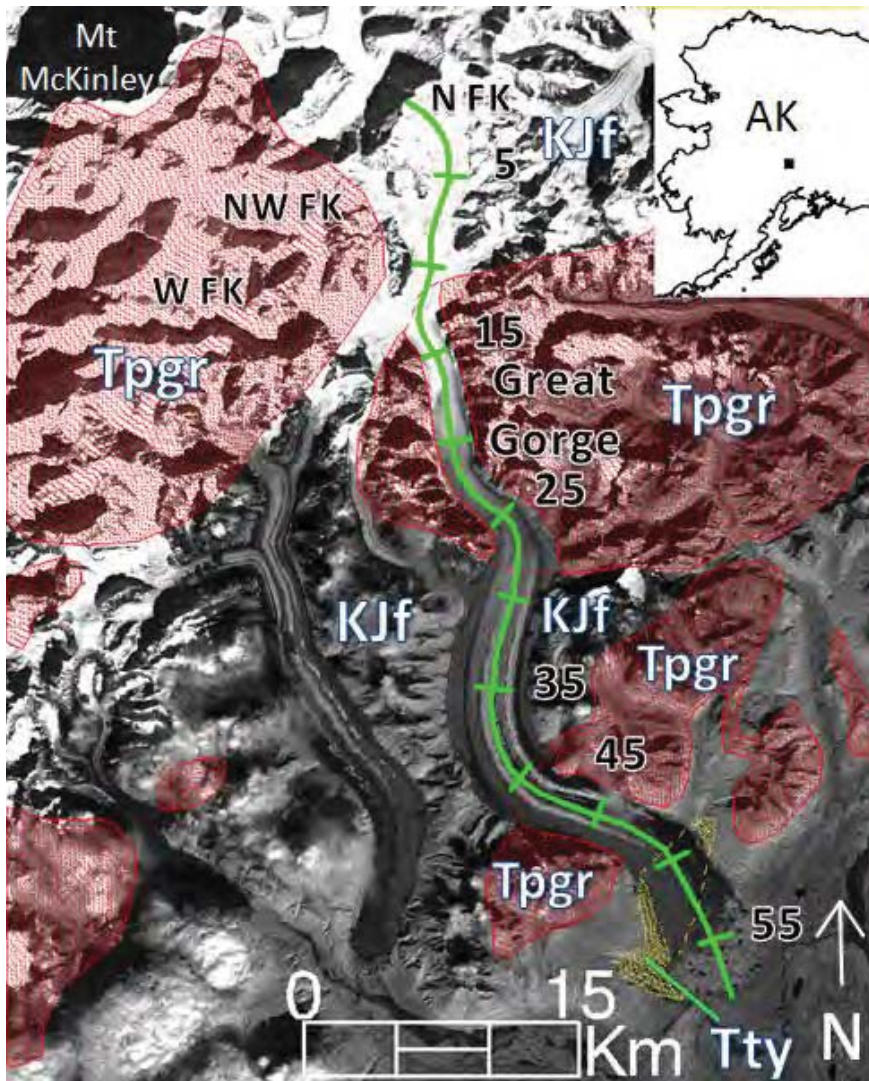
434 Ahn, Y., and I. Howat. 2011. Efficient automated glacier surface velocity measurement from
435 repeat images using Multi-Image/Multichip and null exclusion feature tracking. *IEEE*
436 *Transactions on Geoscience and Remote Sensing*, 49(8), 2838-2846.

- 437 Blake, EW, GKC Clarke, MC Gérin. 1992. Tools for examining subglacial bed deformation.
438 *Journal of Glaciology*, 38(130), 388-396.
- 439 Boulton GS, Dobbie KE, Zatsepin S. 2001. Sediment deformation beneath glaciers and its
440 coupling to the subglacial system. *Quaternary International*, 86, 3-28.
- 441 Burgess, EW, RR Forster, CF Larsen. 2013. Flow velocities of Alaskan glaciers. *Nature*
442 Communications, 4, doi:10.1038/ncomms3146.
- 443 Csejtey, B.Jr, MW Mullen, DP Cox, GD Stricker. 1992. Geology and geochronology of the
444 Healy quadrangle, south-central Alaska: U.S. Geological Survey Miscellaneous
445 Investigations Series Map 1961, 63 p., 2 sheets, scale 1:250,000.
- 446 Fitch, A.J., A. Kadyrov, W.J. Christmas, and J. Kittler. 2002. Orientation correlation, British
447 Machine Vision Conference, 133-142.
- 448 Fowler, A.C., T. Murray, F.S.L. Ng. 2001. Thermally controlled glacier surging. *Journal of*
449 *Glaciology*, 47(159), 527-538.
- 450 Frappé, T. and G.K.C. Clarke. 2007. Slow surge of Trapridge Glacier, Yukon Territory, Canada.
451 *Journal of Geophysical Research*, 112, F03S32, doi:10.1029/2006JF000607.
- 452 Gamble, BM., BL Reed. 1996. Preliminary geologic map of the eastern half of the Lime Hills
453 quadrangle, Alaska: unpublished U.S. Geological Survey map compilation, scale 1:250,000.
- 454 Gesch, D, G Evans, J Mauck, J Hutchinson, WJ Carswell Jr. 2009. *The National Map—*
455 Elevation: U.S. Geological Survey Fact Sheet 2009-3053, 4 p.
- 456 Hall DK, JP Ormsby. 1983. Use of SEASAT synthetic aperture radar and Landsat Multispectral
457 Scanner Subsystem data for Alaskan glaciology studies. *Journal of Geophysical Research*,
458 88(C3), 1597-1607.
- 459 Harrison W.D, L.R. Mayo, D.C. Trabant. 1975. Temperature measurements of Black Rapids
460 Glacier, Alaska, 1973. In Weller, G. and S. A. Bowling, eds. Climate of the Arctic.
461 Proceedings of the 24th Alaska Science Conference. Fairbanks, AK, Univ. of Alaska, 350-
462 352.
- 463 Harrison WD, and A.S. Post 2003. How much do we really know about glacier surging? *Annals*
464 *of Glaciology*, 36(1), 1-6.
- 465 Haug, T., A. Kääb, and P. Skvarca, 2010. Monitoring ice shelf velocities from repeat MODIS
466 and Landsat data – a method study on the Larsen C ice shelf, Antarctic Peninsula, and 10 other
467 ice shelves around Antarctica. *The Cryosphere*, 4, 161-178.
- 468 Heid, T., and A. Kääb. 2012a. Repeat optical satellite images reveal widespread and long term
469 decrease in land-terminating glacier speeds. *The Cryosphere*, 6, 467-478.
- 470 Heid, T., and A. Kääb. 2012b. Evaluation of existing image matching methods for deriving
471 glacier surface displacements globally from optical satellite imagery. *Remote Sensing of*
472 *Environment*, 118, 339-355.

- 473 Jiskoot, H., T. Murray, P. Boyle. 2000. Controls on the distribution of surge-type glaciers in
474 Svalbard. *Journal of Glaciology*, 46(154), 412-422.
- 475 Kamb, B., C.F. Raymond, W.D. Harrison, H. Engelhardt, K.A. Echelmeyer, N. Humphrey, M.M.
476 Brugman, T.Pfeffer. 1985. Glacier surge mechanism: 1982-1983 surge of Variegated Glacier,
477 Alaska. *Science*, 227(4686), 469-479.
- 478 Kavanaugh, JL. 2009. Exploring glacier dynamics with subglacier water pressure pulses:
479 Evidence for self-organized criticality? *Journal of Geophysical Research*, 114, F01021,
480 doi:10.1029/2008JF001036.
- 481 Lee, D.S., J.C. Storey, J. Choate, and R.W. Hayes. 2004. Four years of Landsat-7 on-orbit
482 geometric calibration and performance. *IEEE Trans. on Geoscience and Remote Sensing*,
483 42(12), 2786-2795.
- 484 Leprince, S., S. Barbot, F. Ayoub, and J.P. Avouac. 2007. Automatic and precise ortho-
485 rectification, coregistration, and subpixel correlation of satellite images, application to
486 ground deformation measurements. *IEEE Transactions on Geoscience and Remote Sensing*,
487 45(6), 1529-1558.
- 488 Mayo, LR. 1978. Identification of unstable glaciers intermediate between normal and surging
489 glaciers. Academy of Sciences of the USSR. Section of Glaciology of the Soviet Geophysical
490 Committee and Institute of Geography, Data of Glaciological Studies Chronicle, Discussion,
491 Publication 133, 133-135, Moscow, May 1978.
- 492 Murray, T. 1997. Assessing the paradigm shift: deformable glacier beds. *Quaternary Science
493 Reviews*, 16, 995-1016.
- 494 Murray T., G.W. Stuart, P.J Miller, J. Woodward, A.M. Smith, P.R. Porter, H. Jiskoot. 2000.
495 Glacier surge propagation by thermal evolution at the bed. *Journal of Geophysical Research*,
496 105(B6), 13,491-13,507.
- 497 Murray T, and Porter PR. 2001. Basal conditions beneath a soft-bedded polythermal surge-type
498 glacier: Bakaninbreen, Svalbard. *Quaternary International*, 86, 103-116.
- 499 Murray, T., T. Strozzi, A. Luckman, H. Jiskoot, P. Christakos. 2003. Is there a single surge
500 mechanism? Contrasts in dynamics between glacier surges in Svalbard and other regions.
501 *Journal of Geophysical Research*, 108(B5), 2237, doi:10.1029/2002JB001906.
- 502 Nolan, M. 2003. The "Galloping Glacier" trots: decadal-scale speed oscillations within the
503 quiescent phase. *Annals of Glaciology*, 36, 7-13.
- 504 Nolan M. and K Echelmeyer. 1999. Seismic detection of transient changes beneath Black
505 Rapids Glacier, Alaska, USA: I. Techniques and observations. *Journal of Glaciology*,
506 45(149), 119-131.
- 507 Post, A. 1969. Distribution of surging glaciers in western North America. *Journal of Glaciology*,
508 8(53), 229-240.

- 509 Reed BL, SW Nelson. 1980. Geologic map of the Talkeetna quadrangle, Alaska: U.S. Geological
510 Survey, Miscellaneous Investigation Series Map I-1174, 15 pages, 1 plate, scale 1:250,000.
- 511 Reynolds, O. 1885. On the dilatancy of media composed of rigid particles in contact, with
512 experimental observations. *Philos. Mag.*, 20, 469-481.
- 513 Roush, J.J., C.S. Lingle, R.M. Guritz, D.R. Fatland, and V.A. Voronina. 2003. Surge-front
514 propagation and velocities during the early-1993-95 surge of Bering Glacier, Alaska, USA,
515 from sequential SAR imagery. *Annals of Glaciology*, 36(1), 37-44.
- 516 Scherler D., S. Leprince, and M. Strecker. 2008. Glacier-surface velocities in alpine terrain from
517 optical satellite imagery – Accuracy improvement and quality assessment. *Remote Sensing of
518 Environment*, 112, 3806-3819.
- 519 Shekarforoush M., M. Berthod, and J. Zerubia. 1996. Subpixel image registration by estimating
520 the polyphase decomposition of cross power spectrum. Proceedings: IEEE Computer Society
521 Conference on Computer Vision and Pattern Recognition. San Francisco, CA., USA. June
522 18-20, 1996.
- 523 Shulski, M, HM Mogil. 2009. Alaska's climate and weather. Weatherwise, Jan./Feb., Heldref
524 Publications.
- 525 Solie, DN, WG Gilbert, EE Harris, JT Kline, SA Liss, MS Robinson. 1991. Preliminary geologic
526 map of Tyonek D-6 and eastern Tyonek D-7 quadrangles, Alaska: Alaska Division of
527 Geological and Geophysical Surveys Public-data File 91-10, scale 1:63,360, 15 p., not
528 paginated.
- 529 Stone, DB. 1993. Characterization of the basal hydraulic system of a surge-type glacier:
530 Trapridge Glacier, 1989-1992. Ph.D. Thesis, University of British Columbia, Vancouver,
531 Canada.
- 532 Storey, J.C., and M.J. Choate. 2004. Landsat-5 bumper-mode geometric correction. *IEEE
533 Transactions on Geoscience and Remote Sensing*, 42(12), 2695-2703.
- 534 Truffer M, Harrison WD, Echelmeyer KA. 2000. Glacier motion dominated by processes deep in
535 underlying till. *Journal of Glaciology*, 46(153), 213-221.
- 536 Truffer, M, KA Echelmeyer, WD Harrison. 2001. Implications of till deformation on glacier
537 dynamics. *Journal of Glaciology*, 47(156), 123-134.
- 538 Turrin, J, R.R. Forster, C. Larsen, J. Sauber. 2013. The propagation of a surge front on Bering
539 Glacier, Alaska, 2001-2011. *Annals of Glaciology*, 54(63), 221-227.
- 540 Ward, JD, RS Anderson, PJ Haeussler. 2012. Scaling the Teflon Peaks: Rock type and the
541 generation of extreme relief in the glaciated western Alaska Range. *Journal of Geophysical
542 Research*, 117, F01031, doi:10.1029/2011JF002068.
- 543 Willis, I.C. 1995. Intra-annual variations in glacier motion: a review. *Progress in Physical
544 Geography*, 19(1), 61-106.

545



546

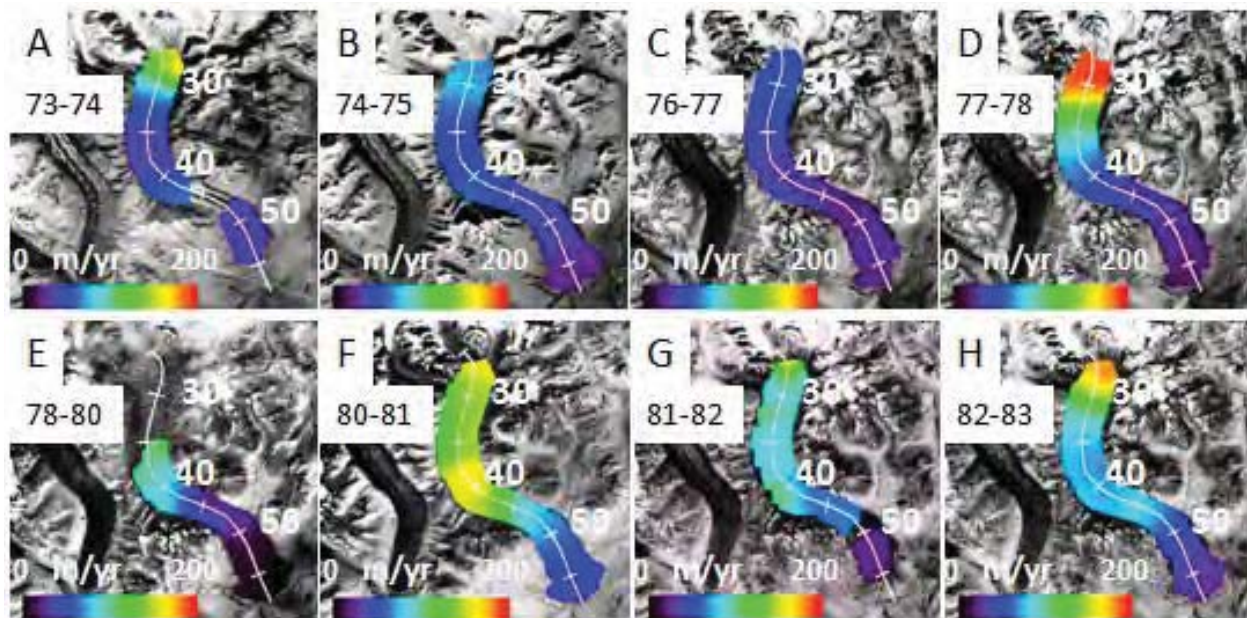
547 **Figure 1.** View of Ruth Glacier in the Alaska Range, Alaska. Red polygons indicate the extent
548 of the granitic Tertiary age bedrock formations in the area, labeled Tpgr. KJf indicates
549 Cretaceous/Jurassic age sedimentary bedrock, and Tty indicates Tertiary age sedimentary
550 bedrock. The green line indicates a transect along the glacier centerline, beginning at the
551 headwall of the north fork, measured in km. The background image was acquired by Landsat-5
552 TM on Sept. 9, 1994. The black rectangle within the inset indicates the position of the
553 background image within Alaska.

554

555

556

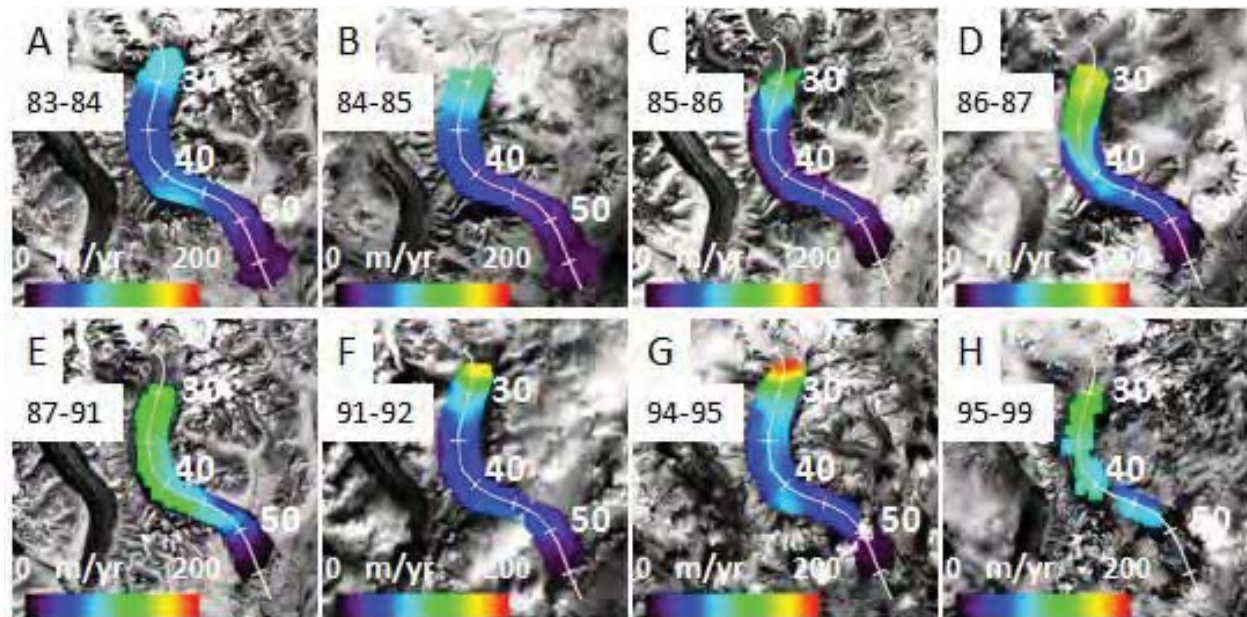
557



558

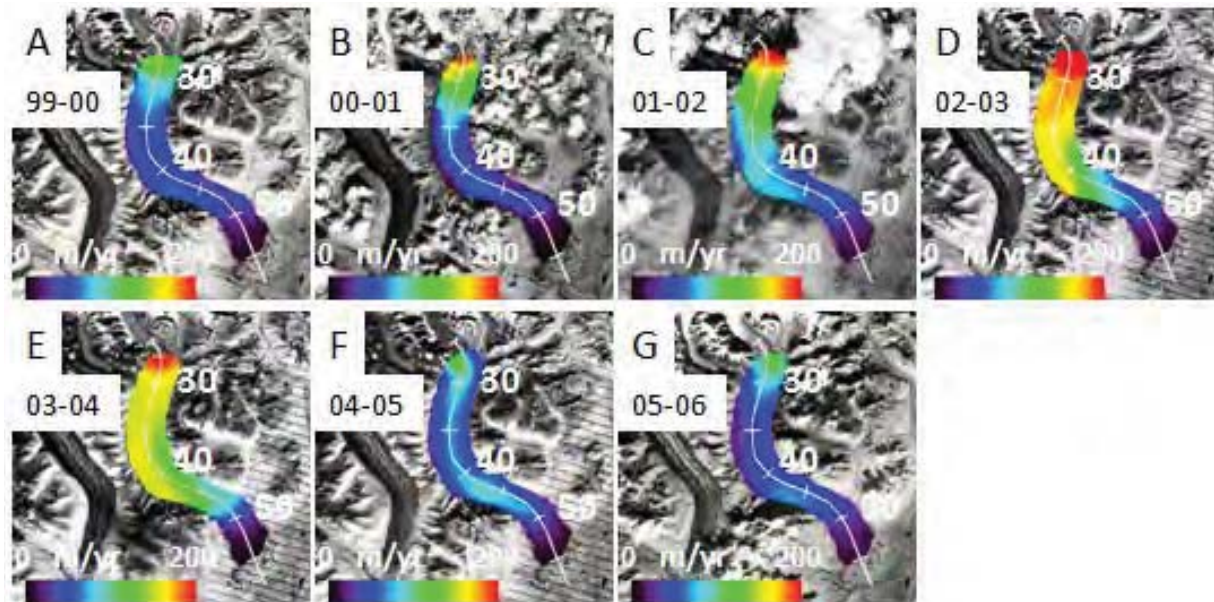
Figure 2. Velocity fields for Ruth Glacier, below the Great Gorge, from 1973 to 1983. Distances along the centerline transect are given in kilometers from the headwall of the north fork (See Fig. 1). A) 1973-1974. B) 1974-1975. C) 1976-1977. D) 1977-1978. E) 1978-1980. F) 1980-1981. G) 1981-1982. H) 1982-1983.

563



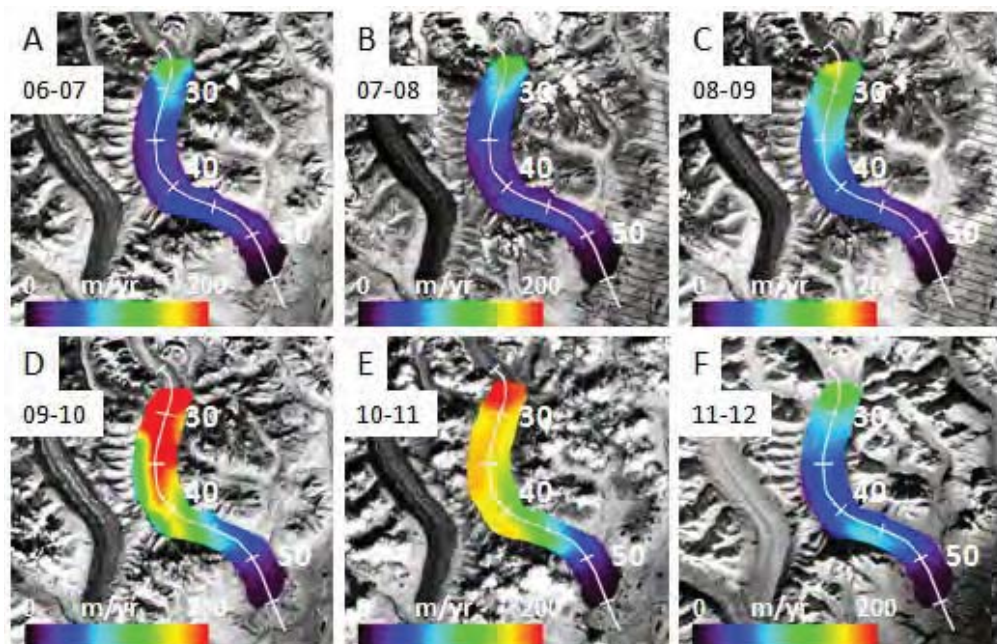
564

Figure 3. Velocity fields for Ruth Glacier, below the Great Gorge, from 1983 to 1999. Distances along the centerline transect are given in kilometers from the headwall of the north fork (See Fig. 1). A) 1983-1984. B) 1984-1985. C) 1985-1986. D) 1986-1987. E) 1987-1991. F) 1991-1992. G) 1994-1995. H) 1995-1999.



569
570
571
572
573

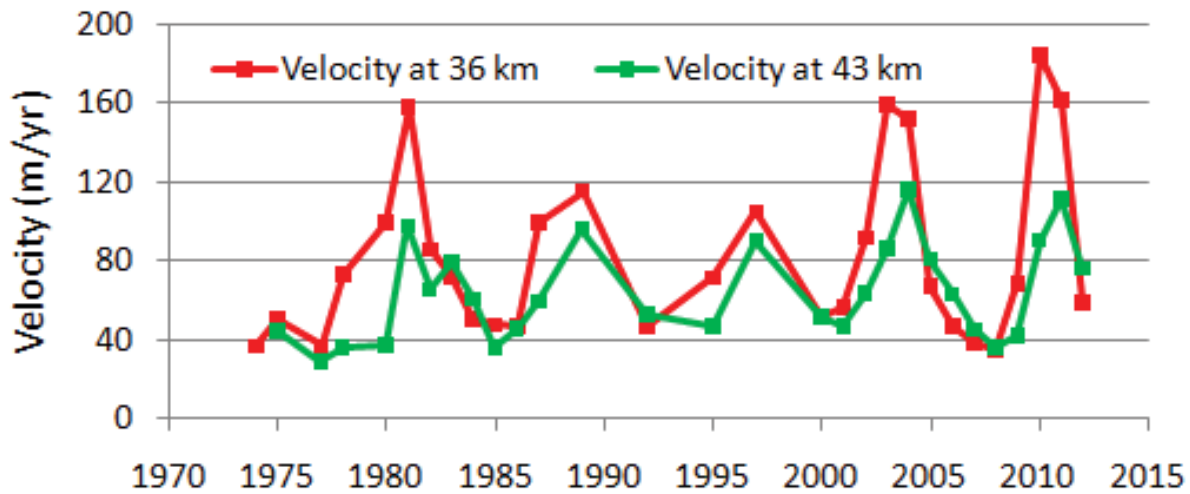
Figure 4. Velocity fields for Ruth Glacier, below the Great Gorge, from 1999 to 2006. Distances along the centerline transect are given in kilometers from the headwall of the north fork (See Fig. 1). A) 1999-2000. B) 2000-2001. C) 2001-2002. D) 2002-2003. E) 2003-2004. F) 2004-2005. G) 2005-2006.



574
575
576
577

Figure 5. Velocity fields for Ruth Glacier, below the Great Gorge, from 2006 to 2012. Distances along the centerline transect are given in kilometers from the headwall of the north fork (See Fig. 1). A) 2006-2007. B) 2007-2008. C) 2008-2009. D) 2009-2010. E) 2010-2011. F) 2011-2012.

578
579



580

581 **Figure 6.** Temporal evolution of ice surface velocity on Ruth Glacier at the 36 km and 43 km
 582 marks from 1973 to 2012. Five pulses are evident, with peaks in velocity in 1981, 1989, 1997,
 583 2003, and 2010, resulting in a characteristic pulse frequency of approximately 7 years.

584

585

586

587

588

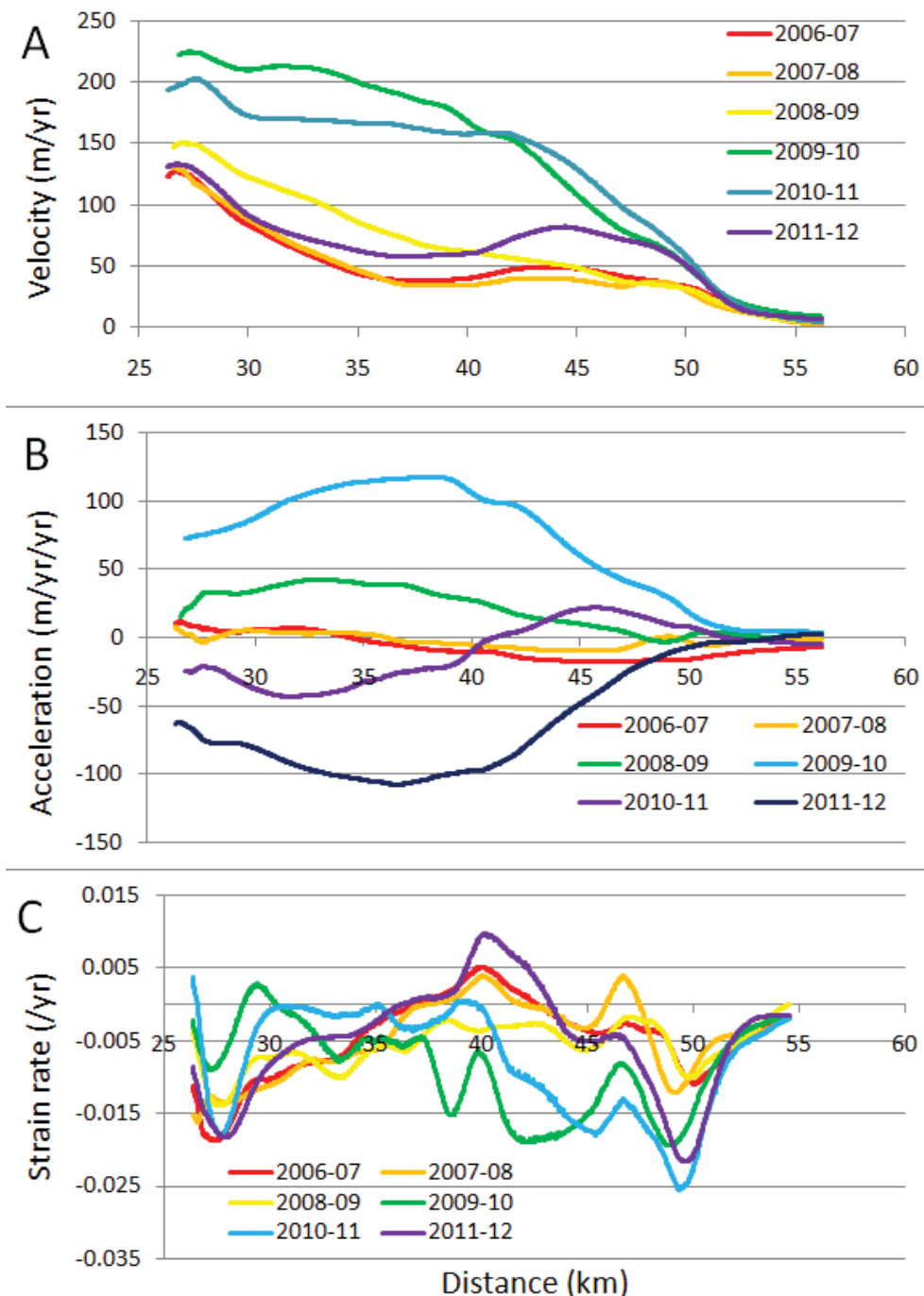
589

590

591

592

593



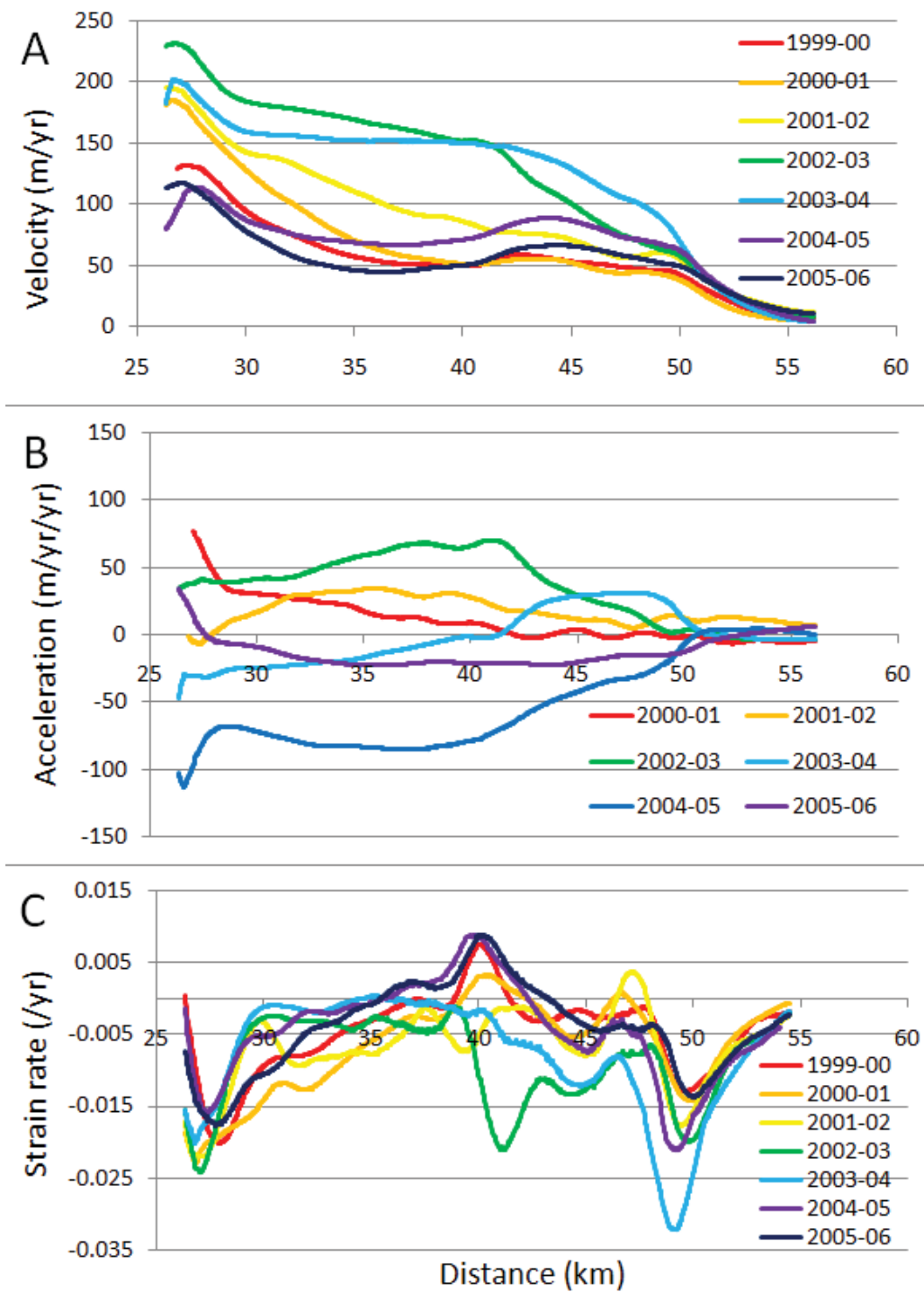
594

595 **Figure 7.** Longitudinal profiles of ice velocity, acceleration, and strain rate along the centerline
 596 transects shown in Figure 5, for the years 2006 to 2012, which surround the 2009-2010 pulse. A)
 597 Ice velocity. B) Ice acceleration. C) Longitudinal strain rate.

598

599

600

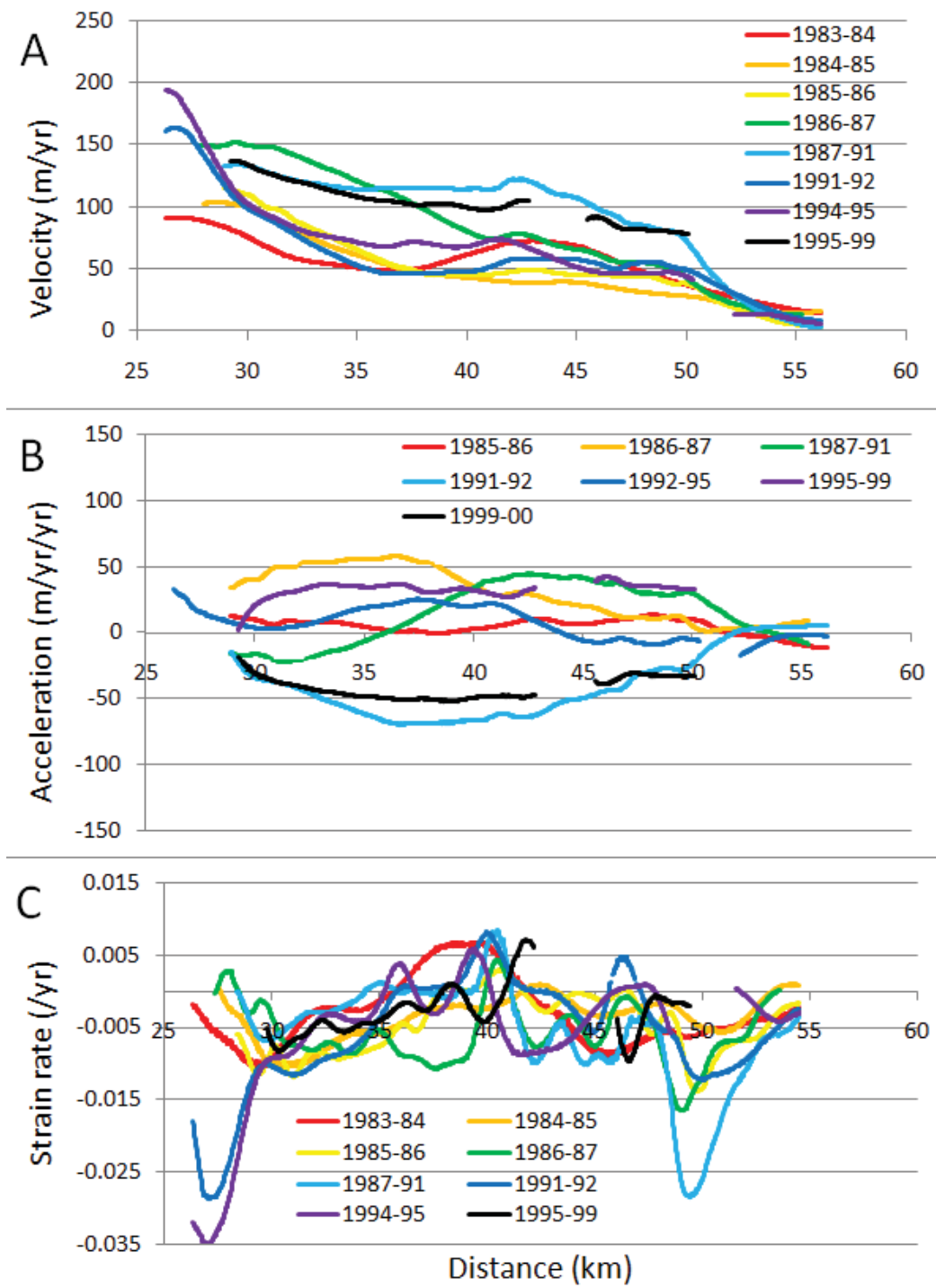


601

602 **Figure 8.** Longitudinal profiles of ice velocity, acceleration, and strain rate along the centerline
 603 transects shown in Figure 4, for the years 1999 to 2006, which surround the 2002-2003 pulse. A)
 604 C) Longitudinal strain rate.

605

606

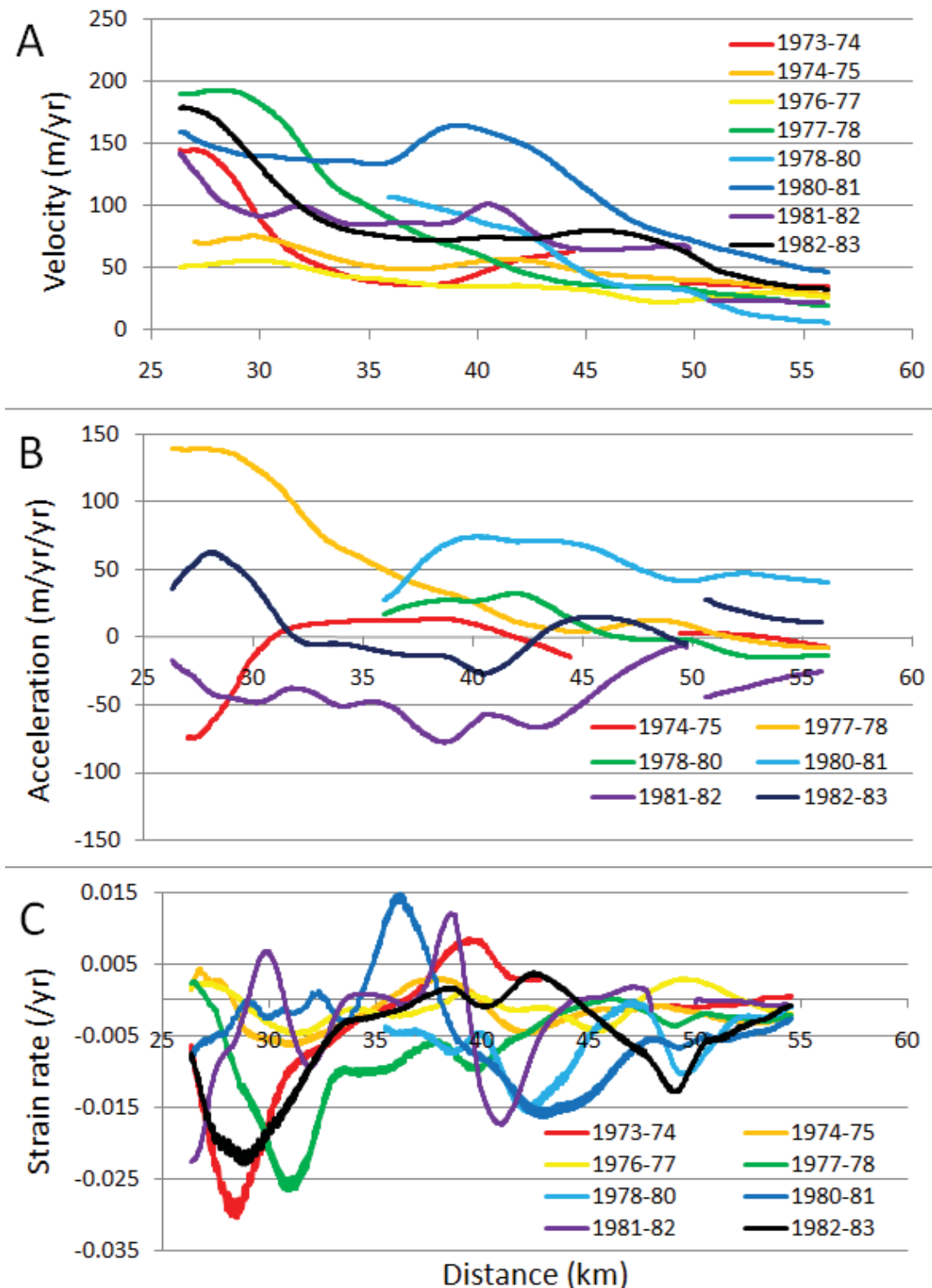


607

608 **Figure 9.** Longitudinal profiles of ice velocity, acceleration, and strain rate along the centerline
 609 transects shown in Figure 3, for the years 1983 to 1999, which surround the 1987-91 and 1995-
 610 1999 pulses. A) Ice velocity. B) Ice acceleration. C) Longitudinal strain rate.

611

612



613

614 **Figure 10.** Longitudinal profiles of ice velocity, acceleration, and strain rate along the centerline
 615 transects shown in Figure 2, for the years 1973 to 1983, which surround the 1980-1981 pulse. A)
 616 B) Ice velocity. B) Ice acceleration. C) Longitudinal strain rate.

617 **Table 1.** Landsat images used in this study. Upon receipt from the U.S. Geological Survey, Multispectral Scanner
618 System images (MSS) have a spatial resolution of 60 meters, and the Thematic Mapper (TM) and Enhanced
619 Thematic Mapper Plus (ETM+) images have spatial resolutions of 30 meters.
620

Image date	Sensor	Spatial resolution (meters)
24 Sept. 1973	MSS 1	60
27 July 1974	MSS 1	60
23 Sept. 1975	MSS 2	60
7 July 1976	MSS 2	60
1 July 1977	MSS 2	60
2 Aug. 1978	MSS 2	60
22 July 1980	MSS 2	60
4 Aug. 1981	MSS 2	60
3 July 1982	MSS 3	60
18 Aug. 1983	MSS 4	60
28 Aug. 1984	MSS 5	60
16 Sept. 1985	MSS 5	60
16 Sept. 1985	TM 5	30
17 July 1986	TM 5	30
21 Aug. 1987	TM 5	30
29 June 1991	TM 5	30
26 Aug. 1992	TM 4	30
9 Sept. 1994	TM 5	30
8 June 1995	TM 5	30
19 June 1999	TM 5	30
16 Aug. 2000	ETM+ 7	30
2 July 2001	ETM+ 7	30
21 July 2002	ETM+ 7	30
9 Aug. 2003	ETM+ 7	30
10 July 2004	ETM+ 7	30
14 Aug. 2005	ETM+ 7	30
10 Sept. 2006	TM 5	30
28 Aug. 2007	TM 5	30
5 July 2008	ETM+ 7	30
8 July 2009	ETM+ 7	30
20 Aug. 2010	TM 5	30
6 July 2011	TM 5	30
18 Oct. 2011	ETM+ 7	30
20 Oct. 2012	ETM+ 7	30

621

622

623

624

625

626

627

628

629 **Table 2.** Georeferencing error and residual error for each image pair used to produce velocity fields. Georeferencing
 630 error represents the initial misalignment between the two satellite images as measured using COSI-Corr, and the
 631 residual error represents their misalignment after the georeferencing error is removed. Image geolocation RMSE is
 632 the root mean square error of the geometric misalignment of each image with respect to ground control points, as
 633 determined during processing of the images before distribution to the public domain. Values given are mean \pm 1
 634 standard deviation.

Image pair	Sensor types	Georef. Error (pixels)	Georef. Error (meters)	Residual Error (pixels)	Residual Error (meters)	Image Geolocation RMSE (pixels, image year)
24 Sept. 1973, 27 July 1974	MSS	0.50 \pm 0.21	36.8 \pm 15.4	0.26 \pm 0.14	19.4 \pm 10.4	0.386, 1973
27 July 1974, 23 Sept. 1975	MSS	0.44 \pm 0.15	23.1 \pm 8.1	0.20 \pm 0.12	10.9 \pm 6.4	0.396, 1974
23 Sept. 1975, 7 July 1976	MSS	0.41 \pm 0.61	14.7 \pm 21.7	0.35 \pm 0.59	12.5 \pm 20.9	0.397, 1975
7 July 1976, 1 July 1977	MSS	0.38 \pm 0.10	22.8 \pm 6.2	0.14 \pm 0.07	8.8 \pm 4.7	0.428, 1976
1 July 1977, 2 Aug. 1978	MSS	0.33 \pm 0.13	18.5 \pm 7.3	0.16 \pm 0.07	9.0 \pm 4.2	0.391, 1977
2 Aug. 1978, 22 July 1980	MSS	0.50 \pm 0.24	30.2 \pm 14.6	0.26 \pm 0.12	15.8 \pm 7.2	0.357, 1978
22 July 1980, 4 Aug. 1981	MSS	0.50 \pm 0.22	30.5 \pm 13.2	0.26 \pm 0.15	15.7 \pm 9.4	0.682, 1980
2 Aug. 1981, 3 July 1982	MSS	0.87 \pm 0.87	28.4 \pm 28.5	0.36 \pm 0.34	21.5 \pm 21.2	0.747, 1981
3 July 1982, 18 Aug. 1983	MSS	0.42 \pm 0.19	23.2 \pm 10.4	0.32 \pm 0.17	17.4 \pm 9.6	0.430, 1982
18 Aug. 1983, 28 Aug. 1984	MSS	0.26 \pm 0.12	15.8 \pm 7.3	0.16 \pm 0.09	10.1 \pm 5.9	0.564, 1983
28 Aug. 1984, 16 Sept. 1985	MSS	0.35 \pm 0.16	21.1 \pm 10.0	0.24 \pm 0.18	14.6 \pm 11.1	0.496, 1984, 0.470, 1985
Average for MSS imagery		0.45 \pm 0.15	24.1 \pm 6.7	0.25 \pm 0.07	14.1 \pm 4.2	0.47 \pm 0.12
16 Sept. 1985, 17 July 1986	TM	0.45 \pm 0.25	16.5 \pm 9.1	0.38 \pm 0.24	13.9 \pm 8.8	0.228, 1985
17 July 1986, 21 Aug. 1987	TM	0.44 \pm 0.13	12.2 \pm 3.7	0.21 \pm 0.15	5.7 \pm 4.3	0.184, 1986
21 Aug. 1987, 29 June 1991	TM	0.20 \pm 0.14	6.2 \pm 4.4	0.16 \pm 0.09	5.0 \pm 2.8	0.155, 1987
29 June 1991, 26 Aug. 1992	TM	0.28 \pm 0.18	7.8 \pm 5.0	0.21 \pm 0.13	5.9 \pm 3.5	0.191, 1991, 0.132, 1992
9 Sept. 1994, 8 June 1995	TM	0.24 \pm 0.16	8.8 \pm 6.1	0.19 \pm 0.13	7.1 \pm 5.0	0.143, 1994
8 June 1995, 19 June 1999	TM	0.21 \pm 0.09	6.5 \pm 2.8	0.13 \pm 0.03	4.0 \pm 1.1	0.154, 1995
19 June 1999, 16 Aug. 2000	TM/ETM+	0.22 \pm 0.16	6.0 \pm 4.5	0.15 \pm 0.13	4.3 \pm 3.7	0.155, 1999
16 Aug. 2000, 2 July 2001	TM	0.20 \pm 0.14	7.0 \pm 4.9	0.17 \pm 0.15	5.8 \pm 5.1	0.119, 2000
2 July 2001, 21 July 2002	TM	0.30 \pm 0.09	9.0 \pm 2.7	0.06 \pm 0.04	1.9 \pm 1.2	0.141, 2001
21 July 2002, 9 Aug. 2003	TM	0.14 \pm 0.10	4.0 \pm 2.9	0.12 \pm 0.11	3.6 \pm 3.3	0.187, 2002
9 Aug. 2003, 10 July 2004	TM	0.13 \pm 0.06	3.9 \pm 1.8	0.11 \pm 0.04	3.3 \pm 1.4	0.125, 2003
10 July 2004, 14 Aug. 2005	TM	0.13 \pm 0.07	4.0 \pm 2.2	0.10 \pm 0.07	3.1 \pm 2.1	0.151, 2004
14 Aug. 2005, 10 Sept. 2006	ETM+/TM	0.26 \pm 0.19	7.2 \pm 5.3	0.24 \pm 0.14	6.6 \pm 3.9	0.121, 2005
10 Sept. 2006, 28 Aug. 2007	TM	0.17 \pm 0.16	5.3 \pm 5.0	0.15 \pm 0.12	4.6 \pm 3.6	0.165, 2006
28 Aug. 2007, 5 July 2008	TM/ETM+	0.18 \pm 0.08	6.5 \pm 2.8	0.16 \pm 0.09	5.7 \pm 3.4	0.127, 2007
5 July 2008, 8 July 2009	TM	0.16 \pm 0.07	4.8 \pm 2.1	0.06 \pm 0.03	2.0 \pm 0.9	0.148, 2008
8 July 2009, 20 Aug. 2010	ETM+/TM	0.18 \pm 0.06	5.6 \pm 1.9	0.09 \pm 0.04	2.7 \pm 1.4	0.139, 2009
20 Aug. 2010, 6 July 2011	TM	0.18 \pm 0.13	5.6 \pm 4.1	0.11 \pm 0.11	3.5 \pm 3.4	0.092, 2010, 0.225, 2011
18 Oct. 2011, 20 Oct. 2012	ETM+	0.21 \pm 0.14	6.3 \pm 4.3	0.18 \pm 0.14	5.5 \pm 4.4	0.243, 2011, 0.290, 2012
Average for TM/ETM+ imagery		0.22 \pm 0.09	7.0 \pm 3.0	0.15 \pm 0.07	4.9 \pm 2.6	0.16 \pm 0.04

